

Topotactic fabrication of transition metal dichalcogenide superconducting nanocircuits

Received: 13 March 2023

Accepted: 7 July 2023

Published online: 18 July 2023

 Check for updates

Xiaohan Wang^{1,5}, Hao Wang^{1,2,5} , Liang Ma^{1,5}, Labao Zhang^{1,2} , Zhuolin Yang¹, Daxing Dong³, Xi Chen⁴ , Haochen Li¹, Yanqiu Guan¹, Biao Zhang¹, Qi Chen¹, Lili Shi¹, Hui Li¹, Zhi Qin¹, Xuecou Tu¹ , Lijian Zhang¹ , Xiaoqing Jia^{1,2} , Jian Chen¹ , Lin Kang^{1,2} & Peiheng Wu^{1,2} 

Superconducting nanocircuits, which are usually fabricated from superconductor films, are the core of superconducting electronic devices. While emerging transition-metal dichalcogenide superconductors (TMDSCs) with exotic properties show promise for exploiting new superconducting mechanisms and applications, their environmental instability leads to a substantial challenge for the nondestructive preparation of TMDSC nanocircuits. Here, we report a universal strategy to fabricate TMDSC nanopatterns via a topotactic conversion method using prepatterned metals as precursors. Typically, robust NbSe₂ meandering nanowires can be controllably manufactured on a wafer scale, by which a superconducting nanowire circuit is principally demonstrated toward potential single photon detection. Moreover, versatile superconducting nanocircuits, *e.g.*, periodical circle/triangle hole arrays and spiral nanowires, can be prepared with selected TMD materials (NbS₂, TiSe₂, or MoTe₂). This work provides a generic approach for fabricating nondestructive TMDSC nanocircuits with precise control, which paves the way for the application of TMDSCs in future electronics.

Since the first discovery of intrinsic superconductivity in exfoliated 2H-NbSe₂ in the 1970s¹, 2D transition metal dichalcogenide superconductors (TMDSCs) have drawn considerable research interest and expedited insight into novel physical properties^{2–9}. Van der Waals heterostructures based on TMDSC mono/few layers have also spawned exotic superconducting phenomena and new physical mechanisms^{10–13}. These novel physical phenomena have also derived many superconducting electronic devices, such as photodetectors¹⁴, nonreciprocal antennas¹⁵, and supercurrent diodes¹⁶. Nanopatterning fabrication is the critical gap in the development of TMDSCs from fundamental research to practical applications^{16–20}. Notably, recent advances in fundamental studies on TMDSCs are predominantly

conducted on mechanically exfoliated flakes and/or restacked heterostructures, which are still far from practical device applications due to their limited size (<100 μm) and suboptimal stability^{3,5,21}.

Recently, large-area TMDSCs have been intensely pursued through a variety of progressive approaches, including chemical intercalation and exfoliation²², chemical vapor deposition (CVD)^{23,24}, and molecular beam epitaxy (MBE)^{25,26}. Strikingly, Lin et al.²⁴ reported a two-step growth of environmentally stable wafer-scale TMDSC films, laying the foundation for the future development of integrated superconducting electronic devices. Superconducting nanocircuits patterned from films play an indispensable role in the function and performance of superconducting electronic devices^{14,27–33}. For

¹Research Institute of Superconductor Electronics, School of Electronic Science and Engineering, College of Engineering and Applied Science, Nanjing University, Nanjing 210023, China. ²Hefei National Laboratory, Hefei 230088, China. ³Department of Applied Physics, Nanjing University of Aeronautics and Astronautics, Nanjing 210016, China. ⁴Department of Physics, Tsinghua University, Beijing 100084, China. ⁵These authors contributed equally: Xiaohan Wang, Hao Wang, Liang Ma. ✉e-mail: wanghao91@nju.edu.cn; Lzhang@nju.edu.cn; phwu@nju.edu.cn

example, in superconducting nanowire single-photon detectors (SNSPDs), ultrathin superconducting films need to be etched into meandered nanowires for ultrahigh detection sensitivity^{34,35}. In addition, patterned superconducting systems have induced many exotic physics, e.g., bosonic metallicity³⁶, and metallic TMDSC gratings³⁷ have been demonstrated to be promising candidates for the near-infrared range. However, despite inspiring achievements, the nondestructive patterning of superconducting nanocircuits on TMDSC films has not been well demonstrated. The multi-step patterning process, involving electron beam lithography and reactive ion etching, inevitably destroys the environmentally unstable TMDSC films. Thus, to advance practical applications in integrated electronics, the development of nondestructive processing of TMDSC nanocircuits is critical but challenging.

Here, we devise a topotactic conversion approach to achieve the nondestructive fabrication of various TMDSC nanocircuits through the chalcogenization of prepatterned transition metals. Typically, multifarious structures (e.g., meandering/spiral nanowires and periodical holey arrays) are patterned on transition metals by electron beam lithography and reaction ion etching, which topotactically transform into targeted TMDSC nanocircuits after annealing in chalcogen atmospheres. A set of microscopies, spectroscopic, and electrical characterizations reveal that the topotactically fabricated NbSe₂ nanowires retain better structural and superconducting properties compared to the counterpart obtained from patterning NbSe₂ films. A demoed device on a NbSe₂ circuit delivers regular critical currents in different widths under different temperatures, demonstrating its high quality and potential for further application in integrated electronics.

Results

Strategies for preparing TMDSC nanocircuits

TMDSCs have many novel phenomena in quantum physics and show potential in both fundamental research and practical applications, for which the fabrication of TMDSC nanocircuits is essential. The traditional top-down patterning strategy that patterns a film into the targeted nanocircuit has been widely applied in the electronic community. However, this process involves a set of chemical treatments, including resist coating, baking, developing, and lift-off in organics, which inevitably destroy the environmentally unstable

TMDSCs. As illustrated in Fig. 1, a TMDSC film is first synthesized by topotactic conversion of the metal film sputtered on a substrate³⁸. Then, the as-prepared film is top-down patterned into specific nanocircuits, e.g., meandered nanowires. This process could result in the generation of oxidized species and vacancies in the TMDSC nanocircuit, which largely deteriorate its structural and superconducting properties. To meet this challenge, a nondestructive topotactic fabrication method is developed. In detail, the metal film is first patterned into selected nanostructures and then chalcogenized into a nanostructured TMDSC through a topotactic conversion procedure. Impressively, all the patterning processes are applied forward to the metal precursors rather than TMDSCs; as a result, nondestructive fabrication of TMDSC nanocircuits can be readily realized.

Characterization of NbSe₂ meandered nanowire

As a prototypical TMDSC, 2H-NbSe₂ has attracted much attention due to its unique out-of-plane or Ising spin-orbit coupling⁴. Here, the non-destructive fabrication of a NbSe₂ meandered nanowire is demonstrated by the proposed topotactic fabrication strategy (defined as TF-NbSe₂). First, a dense Nb film with a thickness of 2 nm (roughness of 0.2 nm) was deposited on the sapphire substrate by magnetron sputtering (Supplementary Fig. 1a). The 2 nm thick Nb film was metallic, and the resistance decreased as the temperature decreased; however, it cannot exhibit superconducting properties at a temperature of approximately 1.8 K, which should be attributed to surface oxidation (Supplementary Fig. 1b)³⁹. The X-ray photoemission spectroscopy (XPS) and time-of-flight secondary ion mass spectrometry results confirm that Nb was partially oxidized into a composite of Nb and Nb₂O₅ after patterning by electron beam lithography and reaction ion etching; consequently, a partially oxidized Nb meandered nanowire with a width of 200 ± 10 nm was prepared (Supplementary Fig. 1c–f). The partially oxidized Nb meandered nanowire was transformed into a NbSe₂ meandered nanowire by topotactic selenization. In the Raman spectrum (Supplementary Fig. 2a), two peaks at 229 and 243 cm⁻¹ can be assigned to the A_{1g} and E_{2g} modes of NbSe₂, respectively, indicating the topotactic transformation of the Nb precursor into NbSe₂^{19,40}. The scanning electron microscopy (SEM) and atomic force microscopy (AFM) images (Fig. 2a and Supplementary Fig. 2b–d) show that a continuous meandered NbSe₂ nanowire is obtained, which has a dense surface and a uniform linewidth. Note that the height of the NbSe₂

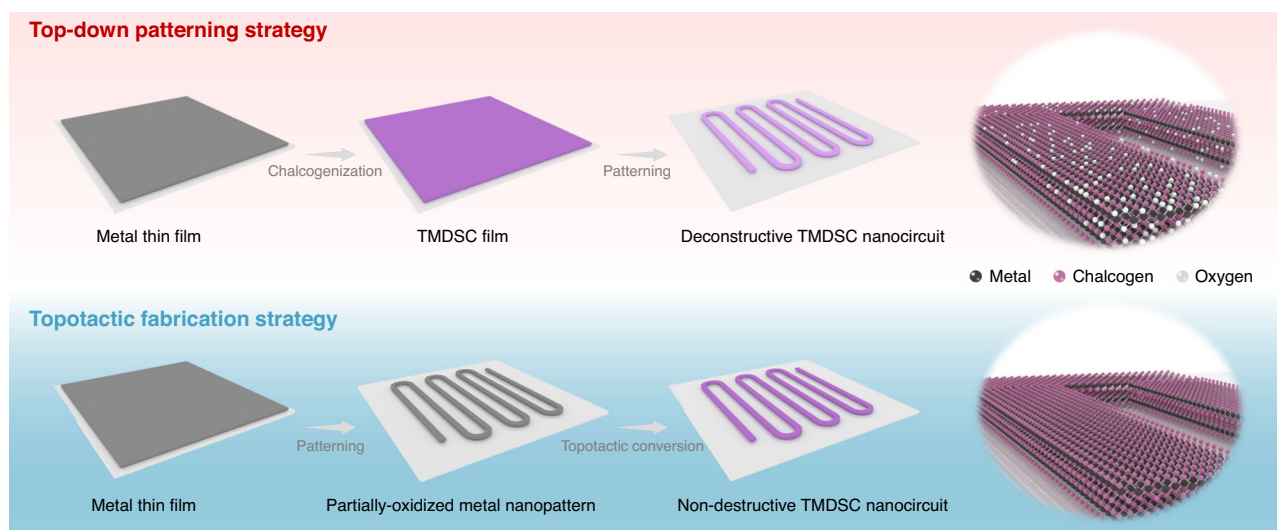


Fig. 1 | Schematic illustrations of top-down patterning and topotactic fabrication strategies for preparing transition metal dichalcogenide superconductors (TMDSC) nanocircuits. The top-down patterning method involves three steps: (i) deposition of metal films on a substrate; (ii) chalcogenization of

metal films into TMDSC films; and (iii) etching of TMDSC films into nanopatterns with severe degradation. In contrast, the topotactic fabrication method topotactically chalcogenizes the prefabricated partially-oxidized metal nanopatterns, which avoids the destruction of the TMDSCs from the patterning process.

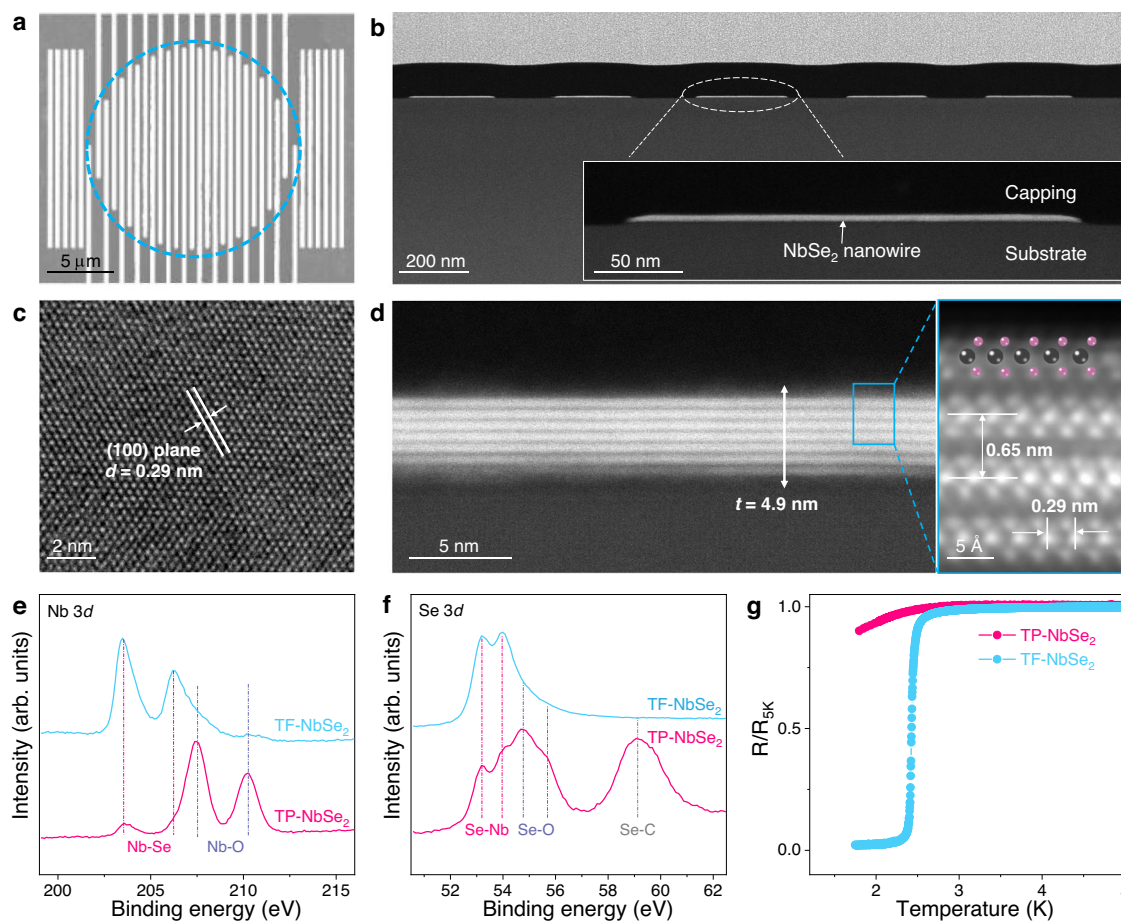


Fig. 2 | Characterization of NbSe₂ meandered nanowire prepared by topotactic fabrication strategy (TF-NbSe₂). **a** Scanning electron microscopy (SEM) image of TF-NbSe₂, in which a gray meandered nanowire on a white background is highlighted by a dashed blue circle. **b** Cross-sectional scanning transmission electron microscopy (STEM) image of TF-NbSe₂ nanowire and inset is the enlarged image of a single TF-NbSe₂ nanowire. **c** In-plane high-resolution transmission electron microscopy (HRTEM) image of TF-NbSe₂ with a lattice distance (d) of 0.29 nm for (100) plane. **d** High-resolution STEM image of TF-NbSe₂ along with enlarged

atomic-resolution display, showing the van der Waals layered structure with a thickness (t) of 4.9 nm and a layer distance of 0.65 nm. The Nb and Se atoms are represented with black and pink spheres, respectively. Core-level Nb 3d (**e**) and Se 3d (**f**) X-ray photoemission spectroscopy (XPS) spectra of TF-NbSe₂ and NbSe₂ prepared by top-down patterning strategy (TP-NbSe₂). The vertical dash lines refer to the bonds below in the same color. **g** Temperature dependence of the resistance for TF-NbSe₂ and TP-NbSe₂. R_{5K} means the resistance at the temperature of 5 K.

nanowire is determined to be ~5 nm, which is 2.2-fold that of the partially-oxidized Nb precursor (2.3 nm). The wafer photography and XRD results demonstrate that the prepatterned Nb precursor is fully and macroscopically transformed into NbSe₂ (Supplementary Fig. 3). Furthermore, the thickness and width of the NbSe₂ nanowires can be precisely controlled by tuning the sputtering time and electron beam lithography parameters (Supplementary Fig. 4).

Aberration-corrected scanning transmission electron microscopy (STEM) was used to reveal the microstructure of NbSe₂. As shown in Fig. 2b, the cross-sectional image of the meandered NbSe₂ nanowire shows a uniform width of 200 nm, and the enlarged image shows the continuity and homogeneity of the TF-NbSe₂. The in-plane high-resolution transmission electron microscopy (HRTEM) image (Fig. 2c) reveals the in-plane atomic arrangement of NbSe₂, in which the lattice distances of 0.29 nm corresponds to the (100) plane. The high-resolution STEM image of TF-NbSe₂ (Fig. 2d) shows the layered structure and typical atomic arrangement of the NbSe₂ crystal without any oxidized species. The layer-by-layer van der Waals structure of NbSe₂, with a layer thickness of 0.65 nm and a total thickness of 4.9 nm^{25,41}, is in agreement with the AFM result. Even at the edge of the TF-NbSe₂ nanowire, the layered structure is clearly observed without distinguishable oxidation (Supplementary Fig. 5). The corresponding EDS mappings further confirm the intact

NbSe₂ composition at the edge of TF-NbSe₂ nanowire with a negligible oxygen signal. For comparison, another meandered NbSe₂ nanowire is prepared by etching a NbSe₂ film, which is derived from traditional top-down patterning (defined as TP-NbSe₂) (Supplementary Fig. 6).

While the two kinds of meandered NbSe₂ nanowires exhibit similar morphologies, their intrinsic properties vary extremely. First, the chemical state and composition of the two samples are examined by XPS. As shown in Fig. 2e, two pairs of peaks at 203.4/206.2 and 207.5/210.3 eV are observed in the Nb 3d XPS spectrum of the TF-NbSe₂ sample, which is attributed to Nb⁴⁺ (NbSe₂) and Nb⁵⁺ (Nb₂O₅), respectively⁴². It should be noted that the slight oxidation in TF-NbSe₂ arises from surface oxidation during XPS measurement. In contrast, the peaks referring to Nb₂O₅ species are in the majority of the Nb 3d XPS spectrum for the TP-NbSe₂ sample. This suggests that TP-NbSe₂ experiences severe oxidation during the patterning process. Based on the area of the signal peak after deconvolution (Supplementary Fig. 7), TF-NbSe₂ is determined to be composed of 93.67% NbSe₂ and 6.33% Nb₂O₅, while TP-NbSe₂ contains 26.7% NbSe₂ and 73.3% Nb₂O₅. The Nb/Se/O ratios are calculated to be 1/1.76/0.30 and 1/0.31/2.12 for TF-NbSe₂ and TP-NbSe₂, respectively (Supplementary Table 1). In addition, two pairs of peaks at 53.3/54.0 and 54.6/55.3 eV, corresponding to Se²⁻ (NbSe₂) and Se⁴⁺ (SeO₂), respectively, are present in the Se 3d XPS

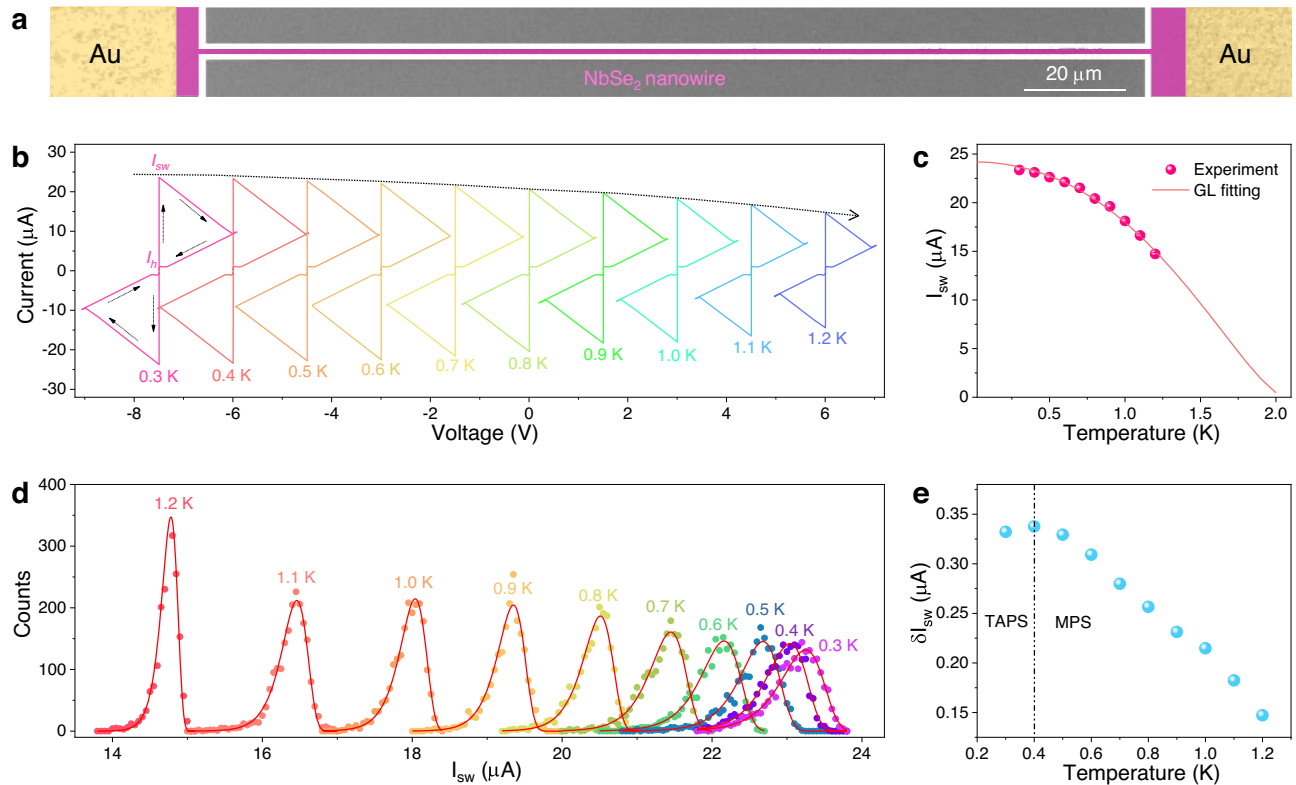


Fig. 3 | Superconducting properties of TF-NbSe₂ nanowire device. **a** SEM image of a 200-nm-wide NbSe₂ nanowire. **b** I - V curves of 200-nm-wide NbSe₂ device under different temperatures. The curves are horizontally offset for clarity, and the arrows represent the bias current (I_b) scan order. **c** The average values of switch current (I_{sw}) for 200-nm-wide NbSe₂ device under different temperatures, which

can be fitted by the Ginzburg–Landau model. **d** Distribution of I_{sw} values for 200-nm-wide NbSe₂ device at different temperatures, which follows Gumbel fitting. **e** Standard deviation I_{sw} (δI_{sw}) of 200-nm-wide NbSe₂ device under different temperatures, in which 400 mK is the crossover temperature of thermally active phased-slip (TAPS) and multiple phase-slip (MPS).

spectra of both TF-NbSe₂ and TP-NbSe₂ (Fig. 2f)⁴³. Obviously, the proportion of SeO₂ in TP-NbSe₂ is much higher than that in TF-NbSe₂, indicating even more serious oxidation of NbSe₂, which is consistent with Nb 3d XPS analyses. Notably, one more peak at 58.9 eV attributed to the C–Se bond emerges in TP-NbSe₂⁴⁴. It is speculated that the organic resist applied in the patterning process can react with NbSe₂ and form C–Se species, which will undoubtedly deteriorate the quality of the NbSe₂ nanocircuit. Notably, TF-NbSe₂ shows competitive quality in structure and composition to NbSe₂ film prepared by selenization of Nb film (Supplementary Fig. 8), indicating that partial oxidation of Nb nanopattern hardly affects the TF-NbSe₂ quality.

To further characterize the superconducting quality, the transport properties at low temperatures of TP-NbSe₂ and TF-NbSe₂ are compared. Figure 2g shows the temperature dependence of the normalized longitudinal resistance at zero magnetic field. For TF-NbSe₂, its resistance begins to plunge at -2.7 K and reaches zero at -2.2 K, suggesting the trigger of superconductivity. In contrast, the resistance of TP-NbSe₂ only slightly decreases as the temperature decreases from 2.9 to 1.8 K, corresponding to a nonsuperconducting state. A TP-NbSe₂ nanowire reported by Mills et al. exhibited a 31.4% decrease in T_c compared to the initial NbSe₂ flake, indicating a substantial degradation in the superconductivity caused by the destructive patterning process¹⁹. Obviously, the NbSe₂ nanopatterns obtained by the topotactic fabrication strategy can retain excellent superconductivity compared to that from top-down patterning.

Demonstration of TF-NbSe₂ nanowire devices

To investigate the feasibility of the topotactic fabrication strategy, a superconducting device based on TF-NbSe₂ nanowires is demoed.

Figure 3a displays the SEM image of the 200-nm-wide NbSe₂ nanowire device with one electrode side connected to the ground electrode (GND), which is systematically evaluated by current–voltage (I - V) characteristics at low temperatures. A measuring circuit is needed to conduct the electrical measurements. As shown in Supplementary Fig. 9, the adjustable voltage source meter (V_s) series connection with resistor R_0 (100 k Ω) provides variable currents to the devices; thus, the bias current (I_b) is input to the DC terminal of the bias-tee and then to the device⁴⁵. Figure 3b displays the I - V curves of the 200-nm-wide NbSe₂ device at different temperatures with a current sweep rate of 0.2 $\mu\text{A s}^{-1}$. Clearly, the device remains in the superconducting state until the I_b exceeds the switch current (I_{sw} , where the superconducting device transitions to a nonsuperconducting state). Once $I_b > I_{sw}$, the device immediately transforms to a normal state and generates resistance. With decreasing I_b below I_{sw} , the device begins with a normal state due to residual Joule heating and finally recovers to the superconducting state at the hysteresis current (I_h). Among them, the I_{sw} value, relative to the number of Cooper pairs, increases with decreasing operation temperature, and the I_h , immune to noise, reflects the equilibrium state between Joule heat and heat dissipation in the nanowire⁴⁶. The I_{sw}/I_h is determined to be over 21 at 1 K (Supplementary Table 2), which is higher than those reported for superconducting nanowires⁴⁷, suggesting promise for application in superconducting single-photon detectors. The relationship between I_{sw} mean values and operation temperature is plotted in Fig. 3c, which can be fitted according to the Ginzburg–Landau (GL) theory⁴⁸. The good agreement between the experimental data and the fittings suggests that the superconductivity of the 200-nm-wide NbSe₂ nanowire basically obeys GL theory, and the T_c of the 200-

nm-wide NbSe₂ nanowire is determined to be approximately 2 K by fitting the GL theory.

Furthermore, phase fluctuations reveal the intrinsic fluctuation of the superconductors and are the cause of the superconducting transition, representing the stability of the system under certain temperatures, that is, the distribution of I_{sw} when the superconductor switches to the normal state. Here, we further performed 2000 I - V sweeps with a sweep rate of 5 nA s⁻¹ to record the distribution of I_{sw} values of the 200-nm-wide NbSe₂ device at different operation temperatures (Supplementary Fig. 10). After frequency counting with a bin size of 50 nA, all the I_{sw} distributions are basically consistent with the Gumbel fitting from 300 mK to 1.2 K (Fig. 3d)⁴⁹. The standard deviation δI_{sw} of each distribution under a certain temperature is calculated and plotted in Fig. 3e. The overall trend follows the conventional phase-slip theory, and δI_{sw} reaches a peak at 400 mK, which decreases with the operating temperature from 400 mK to 1.2 K and slightly decreases after the temperature is below 400 mK. This indicates that 400 mK is the crossover temperature of the thermally active phase-slip (TAPS) and multiple phase-slip (MPS) for the NbSe₂ device^{46,50}. Moreover, NbSe₂ nanowire devices with different widths of 200, 400, 800, and 1000 nm are fabricated and compared (Supplementary Fig. 11). All the relationships between I_{sw} and operation temperature for the other three devices are in accordance with GL theory (Supplementary Fig. 12).

Based on the abovementioned analyses, the traditional top-down patterning approach cannot meet the nondestructive fabrication of TMDSC nanocircuits, which usually suffer from heavy degradation during chemical treatments. To this end, a topotactic fabrication strategy is developed, by which nondestructive TMD (with NbSe₂ as a typical instance) superconducting nanocircuits with tunable parameters (e.g., thickness and width) can be produced through topotactical chalcogenization of prepatterned metal precursors. Comparative characterizations demonstrate the superior structural and superconducting properties of the TF-NbSe₂ nanocircuit. Moreover, a superconducting device is demoted by TF-NbSe₂, exhibiting a typical BCS superconductor. It can be concluded that the topotactic fabrication strategy proposed in this work can overcome the bottleneck of the traditional top-down patterning method when facing the fabrication of environmentally unstable TMDSCs.

The universality of topotactic fabrication strategy

The topotactic fabrication strategy can prevent TMDSCs from suffering damage during the patterning process and realize the non-destructive fabrication of TMDSC nanocircuits for potential device applications. The meandered NbSe₂ superconducting nanowire reaches a length of over 200 μ m with superior continuity and homogeneity. By this topotactic fabrication strategy, the length of nanocircuits is determined by the pre patterning process but is independent of the TMD materials. Strikingly, this method is widely applicable to the nondestructive preparation of diverse TMDSC nanocircuits in different structures and compositions. For structure, hole patterning of superconductors provides a platform to exploit exotic superconductivity fundamentally, e.g., bosonic metallicity³⁶. For material, TiSe₂ is another representative TMDSC with inspiring superconductivity and charge density waves^{51,52}. To prove the universality of the topotactic fabrication strategy, superconducting nanocircuits of circle-hole NbS₂, triangle-hole TiSe₂, and spiral MoTe₂ nanowires are fabricated (Fig. 4 and Supplementary Fig. 13). It is undoubted that this strategy is also applicable to TMD semiconductor nanopatterns for integrated devices (Supplementary Fig. 14). These instances support the promise of the topotactic fabrication strategy in manufacturing high-quality TMDSC nanocircuits for both fundamental research and practical applications.

Discussion

In summary, we have demonstrated a facile and universal strategy for approaching the nondestructive fabrication of TMDSC nanocircuits, including meandered/spiral nanowires and circle/triangle-hole arrays, based on a topotactic conversion mechanism. The strategy employs topotactic chalcogenization of prepatterned metal precursors, which can effectively avoid damage from the patterning process and retain the superconductivity of the TMDSC nanocircuits (demoted by NbSe₂ nanowire devices). Notably, this approach enables the preparation of diverse TMDSC nanocircuits with tunable thickness and width. As such, this scalable fabrication technique ensures the nondestructive production of high-quality TMDSC nanocircuits with precise control. It is beyond doubt that with further development and optimization, more kinds of structures (e.g., in-plane/out-of-plane heterostructures) and compositions (e.g., ternary/quaternary alloys) with striking superconducting properties could be accessible, which will promote the practical application of TMDSCs in functional electronics.

Methods

Fabrication of NbSe₂ meandered nanowires

A topotactic fabrication strategy was developed to prepare non-destructive NbSe₂ meandered nanowires. First, Nb thin films were deposited on single-side polished *c*-plane sapphire substrates (Hefei Kejing) by magnetron sputtering (base pressure <9 × 10⁻⁶ Pa). During the sputtering process, the working power, working pressure, gas flow rate, and deposition rate were set to 100 W, 3 mTorr, 80 sccm, and 0.2 nm s⁻¹, respectively.

Second, the sputtered Nb films were patterned into meandered nanowires. A layer of polymethyl methacrylate (PMMA, Allresist) electron beam resist was spin-coated on the Nb film. After exposure by E-beam lithography (EBL, Raith), the film was developed in methyl isobutyl ketone (MIBK, Allresist) for 90 s and isopropanol (Aladdin, 99%) for 60 s to obtain the desired meandered nanowire structure on PMMA. Then, the exposed film was etched for 40 s by reactive ion etching (RIE, Samco RIE-10NR) with a CF₄ flow of 40 sccm, a working pressure of 4 Pa, and a working power of 100 W. The residual PMMA was removed through a water bath with *N*-methyl pyrrolidone (Aladdin, 99%) at 80 °C for 30 min.

Finally, a two-zone furnace was used for the topotactic selenization of the patterned Nb nanowires. Selenium powder (500 mg) and patterned Nb sample were placed at zones I (upstream) and II (downstream), which were heated to 450 and 800 °C, respectively. Ar (50 sccm) and H₂ (50 sccm) were used as carrier gases. After annealing for 6 min, the furnace was rapidly cooled to room temperature.

For comparison, NbSe₂ meandered nanowires were also prepared by a top-down patterning method. The as-sputtered Nb films were first selenized into NbSe₂ films, followed by patterning into meandered nanowires.

The topotactic fabrication strategy can be adapted to generally fabricate various TMDSC nanopatterns, including circle-hole NbS₂, triangle-hole TiSe₂, and spiral MoTe₂ nanowires. The detailed parameters are listed in Supplementary Tables 3 and 4.

Characterizations

SEM and AFM images were captured by Compact Melin (Zeiss) and Dimension Icon (Bruker), respectively. TEM images were captured by an FEI TECNAI G2 F20 200 kV. Cross-sectional HAADF-STEM images were captured by a Titan Cubed G2 60–300 system. XPS spectra were collected with a Thermo Fisher Es-calab. Raman spectra were obtained on a LabRAM HR Evolution (Horiba) with a 532 nm laser. All samples were fabricated by the EBL system (Raith, EBPG5200) and RIE (Samco RIE-10NR).

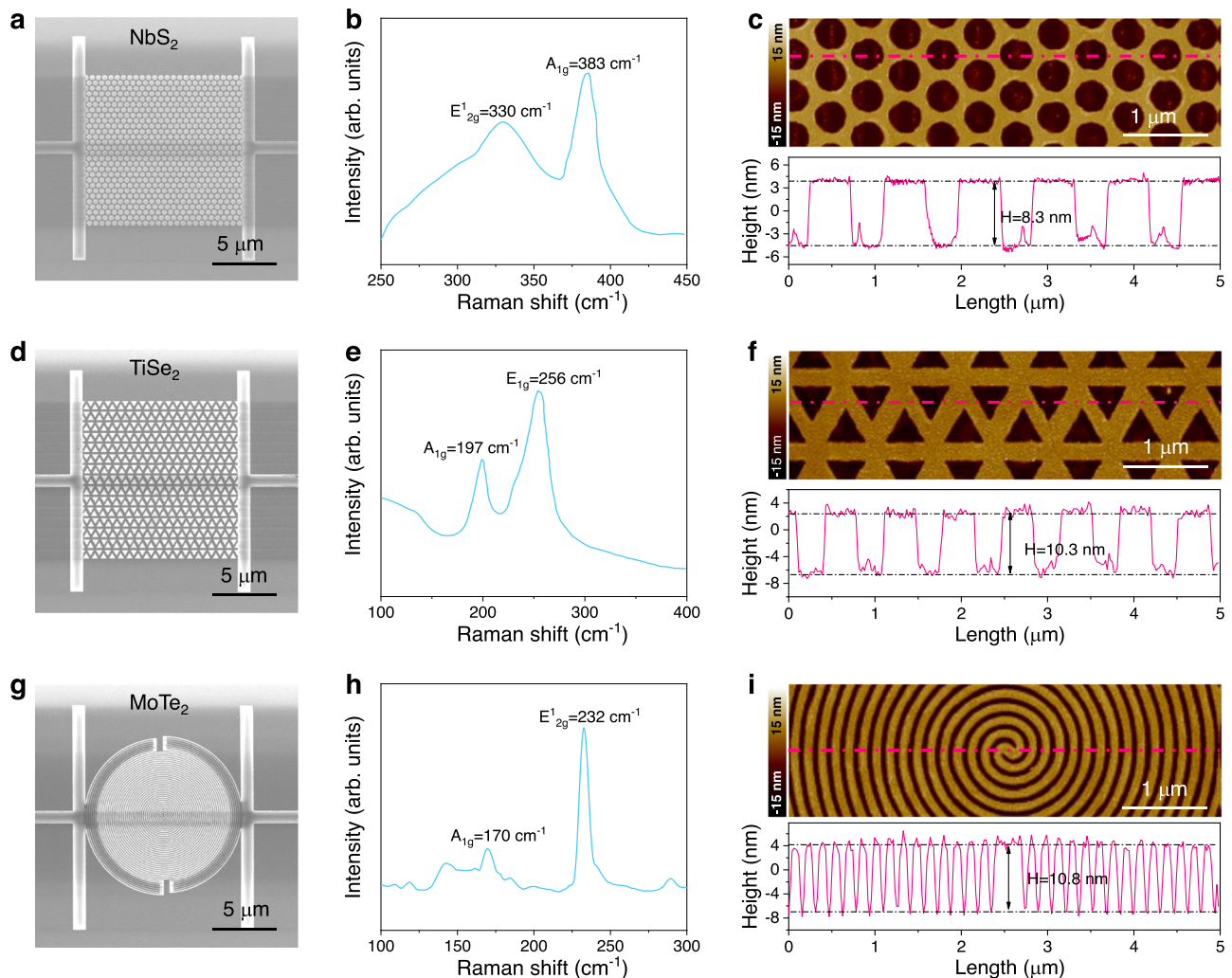


Fig. 4 | Universality of topotactic fabrication strategy. SEM images, Raman spectra, and AFM images of circle-hole NbS₂ (a–c), triangle-hole TiSe₂ (d–f), and spiral MoTe₂ nanowires (g–i). The height (*H*) profiles in c, f, and i are derived from the dashed red line in relative AFM images.

Electrical measurements

The electrical transport characteristics of devices were carried out in the Dilution refrigerating machine for Triton 9 (Oxford Instruments). The measuring circuit includes a digital source meter (keysight 2901) and a T-shaped bias tee. The RF&DC port of the T-shaped Bias-tee is connected to the coaxial cable, leading to devices under extremely low temperatures. The DC port is connected to a digital source meter and the resistor R_0 (100 k Ω) to provide a constant current source, and the RF port is connected to an R_1 (50 Ω) load resistance. Before the measurements, spot welding is used to connect the Ti/Au electrodes to the coaxial cable. The detailed method and corresponding real pictures are presented in Supplementary Fig. 15.

Data availability

The Source Data underlying the figures of this study are provided in the paper. All raw data generated during the current study are available from the corresponding authors upon request. Source data are provided in this paper.

References

- Frindt, R. F. Superconductivity in ultrathin NbSe₂ layers. *Phys. Rev. Lett.* **28**, 299 (1972).
- Calandra, M. & Mauri, F. Charge-density wave and superconducting dome in TiSe₂ from electron-phonon interaction. *Phys. Rev. Lett.* **106**, 196406 (2011).
- Xi, X. X. et al. Ising pairing in superconducting NbSe₂ atomic layers. *Nat. Phys.* **12**, 139–143 (2016).
- Sohn, E. et al. An unusual continuous paramagnetic-limited superconducting phase transition in 2D NbSe₂. *Nat. Mater.* **17**, 504–508 (2018).
- Zheliuk, O. et al. Josephson coupled Ising pairing induced in suspended MoS₂ bilayers by double-side ionic gating. *Nat. Nanotechnol.* **14**, 1123–1128 (2019).
- Liu, X. L., Chong, Y. X., Sharma, R. & Davis, J. C. S. Discovery of a Cooper-pair density wave state in a transition-metal dichalcogenide. *Science* **372**, 1447–1452 (2021).
- Yan, D. et al. NbSeTe—a new layered transition metal dichalcogenide superconductor. *J. Phys. Condens. Matter* **32**, 025702 (2020).
- Zhang, H. X. et al. Tailored Ising superconductivity in intercalated bulk NbSe₂. *Nat. Phys.* **18**, 1425–1430 (2022).
- Xi, X. X., Berger, H., Forro, L., Shan, J. & Mak, K. F. Gate tuning of electronic phase transitions in two-dimensional NbSe₂. *Phys. Rev. Lett.* **117**, 106801 (2016).
- Xu, J. P. et al. Experimental detection of a Majorana mode in the core of a magnetic vortex inside a topological insulator-superconductor Bi₂Te₃/NbSe₂ heterostructure. *Phys. Rev. Lett.* **114**, 017001 (2015).
- Kezilebieke, S. et al. Topological superconductivity in a van der Waals heterostructure. *Nature* **588**, 424–428 (2020).

12. Zhao, W. M. et al. Moire enhanced charge density wave state in twisted 1T-TiTe₂/1T-TiSe₂ heterostructures. *Nat. Mater.* **21**, 284–289 (2022).
13. Yokoi, M. et al. Negative resistance state in superconducting NbSe₂ induced by surface acoustic waves. *Sci. Adv.* **6**, eaba1377 (2020).
14. Walsh, E. D. et al. Josephson junction infrared single-photon detector. *Science* **372**, 409–412 (2021).
15. Zhang, E. Z. et al. Nonreciprocal superconducting NbSe₂ antenna. *Nat. Commun.* **11**, 5634 (2020).
16. Bauriedl, L. et al. Supercurrent diode effect and magnetochiral anisotropy in few-layer NbSe₂. *Nat. Commun.* **13**, 4266 (2022).
17. Jindal, A. et al. Coupled ferroelectricity and superconductivity in bilayer T_d-MoTe₂. *Nature* **613**, 48–52 (2023).
18. de la Barrera, S. C. et al. Tuning Ising superconductivity with layer and spin-orbit coupling in two-dimensional transition-metal dichalcogenides. *Nat. Commun.* **9**, 1427 (2018).
19. Mills, S. A. et al. Single-crystal superconducting nanowires of NbSe₂ fabricated by reactive plasma etching. *Appl. Phys. Lett.* **104**, 052604 (2014).
20. Wang, X. H. et al. All-water etching-free electron beam lithography for on-chip nanomaterials. *ACS Nano* **17**, 4933–4941 (2023).
21. Efetov, D. K. et al. Specular interband Andreev reflections at van der Waals interfaces between graphene and NbSe₂. *Nat. Phys.* **12**, 328–U162 (2016).
22. Li, J. et al. Printable two-dimensional superconducting monolayers. *Nat. Mater.* **20**, 181–187 (2021).
23. Wang, H. et al. High-quality monolayer superconductor NbSe₂ grown by chemical vapour deposition. *Nat. Commun.* **8**, 394 (2017).
24. Lin, H. H. et al. Growth of environmentally stable transition metal selenide films. *Nat. Mater.* **18**, 602–607 (2019).
25. Zhao, K. et al. Disorder-induced multifractal superconductivity in monolayer niobium dichalcogenides. *Nat. Phys.* **15**, 904–910 (2019).
26. Chen, P. et al. Charge density wave transition in single-layer titanium diselenide. *Nat. Commun.* **6**, 8943 (2015).
27. Arute, F. et al. Quantum supremacy using a programmable superconducting processor. *Nature* **574**, 505–510 (2019).
28. Wang, F. F. et al. In vivo non-invasive confocal fluorescence imaging beyond 1,700 nm using superconducting nanowire single-photon detectors. *Nat. Nanotechnol.* **17**, 653–660 (2022).
29. Gol'tsman, G. N. et al. Picosecond superconducting single-photon optical detector. *Appl. Phys. Lett.* **79**, 705–707 (2001).
30. Mazin, B. A. et al. Position sensitive x-ray spectrophotometer using microwave kinetic inductance detectors. *Appl. Phys. Lett.* **89**, 222507 (2006).
31. Fagaly, R. L. Superconducting quantum interference device instruments and applications. *Rev. Sci. Instrum.* **77**, 101101 (2006).
32. Ullom, J. N. & Bennett, D. A. Review of superconducting transition-edge sensors for X-ray and gamma-ray spectroscopy. *Supercond. Sci. Tech.* **28**, 084003 (2015).
33. Shurakov, A., Lobanov, Y. & Goltzman, G. Superconducting hot-electron bolometer: from the discovery of hot-electron phenomena to practical applications. *Supercond. Sci. Tech.* **29**, 023001 (2015).
34. Zadeh, I. E. et al. Superconducting nanowire single-photon detectors: a perspective on evolution, state-of-the-art, future developments, and applications. *Appl. Phys. Lett.* **118**, 190502 (2021).
35. Guan, Y. et al. SNSPD array with single-channel readout based on compressive sensing. *ACS Photonics* **9**, 3102–3109 (2022).
36. Yang, C. et al. Signatures of a strange metal in a bosonic system. *Nature* **601**, 205–210 (2022).
37. Zhao, M. et al. Electrostatically tunable near-infrared plasmonic resonances in solution-processed atomically thin NbSe₂. *Adv. Mater.* **33**, e2101950 (2021).
38. Xiao, X., Wang, H., Urbankowski, P. & Gogotsi, Y. Topochemical synthesis of 2D materials. *Chem. Soc. Rev.* **47**, 8744–8765 (2018).
39. Lin, H. H. et al. Tunability of the superconductivity of NbSe₂ films grown by two-step vapor deposition. *Molecules* **28**, 1059 (2023).
40. Zhou, J. et al. A library of atomically thin metal chalcogenides. *Nature* **556**, 355–359 (2018).
41. Chen, C. et al. Strain-controlled superconductivity in few-layer NbSe₂. *ACS Appl. Mater. Inter.* **12**, 38744–38750 (2020).
42. Park, S. et al. Tailoring domain morphology in monolayer NbSe₂ and W_xNb_{1-x}Se₂ heterostructure. *ACS Nano* **14**, 8784–8792 (2020).
43. Park, H., Kim, J. Y., Oh, J. Y. & Lee, T. I. Long-term stable NbSe₂ nanosheet aqueous ink for printable electronics. *Appl. Surf. Sci.* **504**, 144342 (2020).
44. Liu, L. et al. A stable and ultrafast K ion storage anode based on phase-engineered MoSe₂. *Chem. Commun.* **57**, 3885–3888 (2021).
45. Gaggero, A. et al. Amplitude-multiplexed readout of single photon detectors based on superconducting nanowires. *Optica* **6**, 823–828 (2019).
46. Zhang, B. et al. Photon-assisted phase slips in superconducting nanowires. *Phys. Rev. Appl.* **17**, 014032 (2022).
47. Chen, Q. et al. Suppression of superconductivity dominated by proximity effect in amorphous MoSi nanobelts. *Phys. Rev. B* **105**, 014516 (2022).
48. Il'in, K., Siegel, M., Semenov, A., Engel, A. & Hübers, H. W. Critical current of Nb and NbN thin-film structures: the cross-section dependence. *Phys. Status Solidi C* **2**, 1680–1687 (2005).
49. Li, P. et al. Switching currents limited by single phase slips in one-dimensional superconducting Al nanowires. *Phys. Rev. Lett.* **107**, 137004 (2011).
50. Puglia, C., De Simoni, G. & Giazotto, F. Electrostatic control of phase slips in Ti Josephson nanotransistors. *Phys. Rev. Appl.* **13**, 054026 (2020).
51. Joe, Y. I. et al. Emergence of charge density wave domain walls above the superconducting dome in 1T-TiSe₂. *Nat. Phys.* **10**, 421–425 (2014).
52. Sun, L. et al. Suppression of the charge density wave state in two-dimensional 1T-TiSe₂ by atmospheric oxidation. *Angew. Chem. Int. Ed.* **56**, 8981–8985 (2017).

Acknowledgements

This work was supported by the Natural Science Foundation of Jiangsu Province (No. BK20210177 (H.W.)), the Innovation Program for Quantum Science and Technology (No. 2021ZD0303401 (L.K.)), the National Natural Science Foundation of China (Nos. 12033002 (L.Z.), 62101240 (H.W.), 62071218 (X.J.), and 62288101 (P.W.)), the Key-Area Research and Development Program of Guangdong Province (2020B0303020001 (L.Z.)), the Priority Academic Program Development of Jiangsu Higher Education Institutions (PAPD) and the Jiangsu Provincial Key Laboratory of Advanced Manipulating Technique of Electromagnetic Waves.

Author contributions

H.W., La.Z., and P.W. conceived the study. X.W., L.M., Z.Y., Ha.L., Y.G., B.Z., Q.C., L.S., Hu.L., and Z.Q. performed experiments. D.D., X.C., X.T., Li.Z., X.J., J.C., and L.K. analyzed data. X.W., H.W., La.Z., and P.W. wrote the paper, with all authors editing and approving the final version.

Competing interests

The authors declare no competing interests.

Additional information

Supplementary information The online version contains supplementary material available at <https://doi.org/10.1038/s41467-023-39997-y>.

Correspondence and requests for materials should be addressed to Hao Wang, Labao Zhang or Peiheng Wu.

Peer review information *Nature Communications* thanks Huixia Luo and the other anonymous reviewer(s) for their contribution to the peer review of this work. A peer review file is available.

Reprints and permissions information is available at <http://www.nature.com/reprints>

Publisher's note Springer Nature remains neutral with regard to jurisdictional claims in published maps and institutional affiliations.

Open Access This article is licensed under a Creative Commons Attribution 4.0 International License, which permits use, sharing, adaptation, distribution and reproduction in any medium or format, as long as you give appropriate credit to the original author(s) and the source, provide a link to the Creative Commons licence, and indicate if changes were made. The images or other third party material in this article are included in the article's Creative Commons licence, unless indicated otherwise in a credit line to the material. If material is not included in the article's Creative Commons licence and your intended use is not permitted by statutory regulation or exceeds the permitted use, you will need to obtain permission directly from the copyright holder. To view a copy of this licence, visit <http://creativecommons.org/licenses/by/4.0/>.

© The Author(s) 2023